An Improved Adaptive Sliding Mode Observer for Middle- and High-Speed Rotor Tracking

Wenjun Xu, Shaocheng Qu, *Member, IEEE*, Liang Zhao, and Hongrui Zhang

***Abstract*—In this article, a sensorless field-oriented vector control strategy combined with an improved adaptive sliding mode observer and a back electromotive force (back EMF) observer is presented for a surface permanent magnet synchronous motor. First, based on a sliding mode, a current adaptive observer with estimation of back EMF is proposed to obtain the error of the back EMF, which can reduce system chattering. Then, a back EMF observer based on the back EMF error is constructed to adaptively track the rotor speed and position, which avoids complicated computation. Moreover, the stability of two observers is proved by using the Lyapunov stability theory. Finally, some simulations and experiments are given to show that the proposed method can track the changes of rotor speed and position with good characters, such as fast convergence, little chattering, and good robustness.**

***Index Terms*—Back electromotive force (back EMF), improved adaptive sliding mode observer (IASMO), sensorless control, surface permanent magnet synchronous motor (SPMSM).**

I. Introduction

SURFACE permanent magnet synchronous motors (SPMSMs) are widely used in medical equipment, industrial automation, household appliances, aerospace, unmanned aerial vehicle, and other fields for its advantages of light weight, small size, high efficiency, good reliability, easy control, and wide speed range [1]. On account of its nonlinearity, multicoupling, and time-varying characteristics, appropriate control strategies are required to achieve good control performance [2]. In traditional vector control systems, the rotor speed and position are measured by mechanical sensors such as photoelectric encoder and rotary transformer, which not only increase the cost of system hardware, but also reduce the system reliability [3], [4]. With the rapid development of microcomputer technology, low-cost and high-performance digital processors enable many complex algorithms of sensorless technology to be achieved [5], [6].

Manuscript received December 21, 2019; revised March 16, 2020 and May 8, 2020; accepted June 3, 2020. Date of publication June 16, 2020; date of current version September 4, 2020. This work was supported in part by the National Natural Science Foundation of China under Grant 61673190/F030101 and in part by the Central China Normal University through the Self-Determined Research Funds under Grant CCNU15A02060. Recommended for publication by Associate Editor C. K. Tse. *(Corresponding author: Shaocheng Qu.)*

The authors are with the Department of Electronics and Information Engineering College of Physical Science and TechnologyCentral China Normal University, Wuhan 430079, China (e-mail: xuwenjun@mails.ccnu.edu.cn; qushaocheng@mail.ccnu.edu.cn; zhaoliang@mails.ccnu.edu.cn; zhr@mails.ccnu.edu.cn).

Color versions of one or more of the figures in this article are available online at https://ieeexplore.ieee.org.

Digital Object Identifier 10.1109/TPEL.2020.3000785

In recent years, the research of sensorless control technology has become one of the most popular fields in the control technology of PMSM. According to the speed range, the method of sensorless control can be divided into two categories. One is the middle- and high-speed sensorless control method, including direct estimation method, model reference adaptive system (MRAS), and extended Kalman filter [2], [7], [8]. The other is the low-speed sensorless control strategy, tracking the rotor salient pole through injecting high-frequency signals [9], [10].

However, direct estimation method uses the basic electromagnetic relationship of PMSM to obtain the rotor position information, which is sensitive to motor parameters. Moreover, the system error is large and the robustness is poor due to the uncertainty of motor parameters in operation. MRAS is a parameter identification method based on stability theory, which takes unknown parameter equations as an adjustable model. As MRAS does not completely get rid of the dependence on the parameters, the adjustment of parameters is troublesome and the calculation intensity is high [11]. Extended Kalman filter can effectively reduce the disturbance of external disturbance, which works for motors with high dynamic drive system, but its algorithm brings large computation costs and requires high performance of processors [12]–[14]. The high-frequency injection method can effectively observe the rotor position in the low-speed field and solve the salient pole effect of PMSM, but it has narrow application range and easily causes additional high-frequency voltage or current noise [15], [16]. Sliding mode observer (SMO) is independent of the parameters of the SPMSM and external disturbances, so it can ensure the stability and robustness of the system. Moreover, the control algorithm of SMO is simple and easy to be implemented. However, owing to the switching attribute of sliding mode control, the discontinuity of internal control of the system will cause chattering phenomenon and affect the accuracy of control system, even damage devices. Although the chattering cannot be eliminated completely, it can be reduced as much as possible [17], [18].

Much research has been carried out on the reduction of the chattering effect caused by SMO [19]–[21]. The sigmoid or hyperbolic tangent function combined with low-pass filter is usually used to replace the traditional signum function, which leads to the phase shift and low accuracy in the system [22]. In [23], an iterative SMO for sensorless control is proposed to make the system robust against disturbance and it can adapt the variations of the motor parameters. And in [24], a high-speed SMO for the sensorless PMSM control is introduced to overcome the sensitivity of the parameter change through

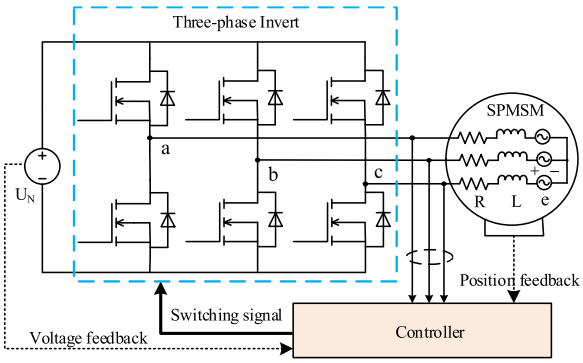

Fig. 1. Block diagram of SPMSM drive system.

observing the variation in the stator resistance. However, after extracting the back EMF information by SMO, the method of calculating the rotor position and angular velocity, which uses arctangent function and differential equation, will introduce high-frequency noise of the system and then, even destroy the stability of the system. There is also a common approach to extract the rotor speed and position information by phase-locked loop, which can filter the high-frequency noise of the system and quickly track the change of the rotor information [25]–[27]. But this method is easily affected by the harmonic component of the system and leads to low accuracy of tracking.

To solve the above-mentioned problems, a sensorless field-oriented vector control (FOC) based on an improved adaptive SMO (IASMO) is proposed to achieve the high performance for the SPMSM. First, an adaptive algorithm and sliding mode current observer are integrated to estimate the error of back EMF. Then, a back EMF observer is designed to observe the rotor speed and position, which can reduce system chattering originating from the excessive sliding mode coefficient in traditional ASMO. Finally, the proposed method can improve the system accuracy with good characters, such as fast response, little chattering, and good robustness; then, these performances of the IASMO are verified by simulations and experiments.

II. SPMSM Drive Model

In the two-phase $(\alpha-\beta)$ stationary coordinate system, the internal electrical structure of SPMSM can be composed of winding resistance R_s, winding inductance L_s, back EMF $\mathbf{e_s}$, and phase voltages $\mathbf{u_s}$. Then, the block diagram of SPMSM drive system is shown in Fig. 1.

Equivalent voltage equation in static coordinate system is obtained as [30]

$$\mathbf{u_s} = R_s\mathbf{i_s} + L_s\frac{d}{dt}\mathbf{i_s} + \mathbf{e_s} \tag{1}$$

where $\mathbf{e_s} = [e_\alpha, e_\beta]^T$, $\mathbf{i_s} = [i_\alpha, i_\beta]^T$, $\mathbf{u_s} = [u_\alpha, u_\beta]^T$; i_α, i_β, e_α, e_β, and u_α, u_β are the stator currents, back EMF signals, and phase voltages for $\alpha-\beta$ axis, respectively. Thus, the state equation of stator current is obtained as [28]

$$\begin{cases} \frac{d}{dt}i_\alpha = -\frac{R_s}{L_s}i_\alpha + \frac{1}{L_s}u_\alpha - \frac{1}{L_s}e_\alpha \\ \frac{d}{dt}i_\beta = -\frac{R_s}{L_s}i_\beta + \frac{1}{L_s}u_\beta - \frac{1}{L_s}e_\beta. \end{cases} \tag{2}$$

On the other hand, the back EMF equation can be expressed as

$$\begin{cases} e_\alpha = -\omega_e\psi_f \sin\theta_e \\ e_\beta = \omega_e\psi_f \cos\theta_e \end{cases} \tag{3}$$

where ψ_f is the flux linkage of the SPMSM,θ_e is the electrical rotor position, and ω_e is the electrical angular speed.

III. Design of an IASMO

A. Design of a New Sliding Mode Current Observer

According to the sliding mode variable structure theory, the sliding mode function $\mathbf{S_n}$ is constructed as [28]

$$\mathbf{S_n} = \begin{bmatrix} S_\alpha \\ S_\beta \end{bmatrix} = \tilde{\mathbf{i}}_\mathbf{s} + \chi\int_0^t \tilde{\mathbf{i}}_\mathbf{s}d\tau \tag{4}$$

where $\tilde{\mathbf{i}}_\mathbf{s} = \begin{bmatrix} \hat{i}_\alpha - i_\alpha \\ \hat{i}_\beta - i_\beta \end{bmatrix} \triangleq \begin{bmatrix} \tilde{i}_\alpha \\ \tilde{i}_\beta \end{bmatrix}$, and $\hat{i}_\alpha$ and $\hat{i}_\beta$ are the estimated currents of the $\alpha-\beta$ axis, respectively; $\tilde{i}_\alpha$and $\tilde{i}_\beta$ represent the error between estimated and actual stator current in the stationary reference frame, respectively, and χ is a constant with $0 < \chi < \frac{R_s}{L_s}$. The sliding mode function (4), which consists of the stator current error and the integral of current error in a sampling period, will suppress chattering when the sliding mode surface is reached in the unit sampling period.

In order to further reduce the high-frequency chattering phenomenon, the signum function and low-pass filter links are replaced by the hyperbolic tangent function as follows:

$$H(x) = \frac{e^{ax} - e^{-ax}}{e^{ax} + e^{-ax}} \tag{5}$$

which is smooth and continuous; a is a constant, which will affect the thickness of boundary layer and the convergence rate of the observer designed later. Obviously, the range of function (5) is $(-1, 1)$, while the signum function is either -1 or 1. Under the same conditions, the larger the value of a, the smaller the thickness of the boundary layer, and the faster the convergence rate of (5).

According to (2), a new state equation of current observer based on sliding mode can be constructed as

$$\begin{cases} \frac{d}{dt}\hat{i}_\alpha = -\frac{R_s}{L_s}\hat{i}_\alpha + \frac{1}{L_s}u_\alpha - \frac{1}{L_s}\hat{e}_\alpha - \frac{k_\alpha(t)}{L_s}H(S_\alpha) \\ \frac{d}{dt}\hat{i}_\beta = -\frac{R_s}{L_s}\hat{i}_\beta + \frac{1}{L_s}u_\beta - \frac{1}{L_s}\hat{e}_\beta - \frac{k_\beta(t)}{L_s}H(S_\beta) \end{cases} \tag{6}$$

where $\hat{e}_\alpha$ and $\hat{e}_\beta$ are the estimated back EMF signals of $\alpha-\beta$ axes during rotor operation, and $k_\alpha(t)$,$k_\beta(t)$ are the α, β axes adaptive gain of SMO, respectively. And the adaptive algorithm is designed as follows:

$$\begin{cases} \dot{k}_i(t) = K_0\,|S_i| & |S_i| \neq 0 \\ k_i(t) = K_1|\phi|^{\frac{1}{2}} & |S_i| = 0 \\ \tau\dot{\phi} + \phi = H(S_i) \\ i = \alpha, \beta \end{cases} \tag{7}$$

where K_0, τ is the positive constant, K_1 is the gain value of $k_i(t_r)$ with $k_i(0) > 0$, and t_r is the reaching time when S_i reaches zero from$S_i \neq 0$, and ϕ is the average of $H(S_i)$ [29].

Let $\mathbf{k_n}(t) = [k_\alpha(t), k_\beta(t)]^T$, $\tilde{\mathbf{k}}_\mathbf{n}(t) = [K^* - k_\alpha(t), K^* - k_\beta(t)]^T$, where K^* is the positive constant and exists for

$$K^* \geq \max(k_\alpha(t), k_\beta(t)) \forall t > 0. \tag{8}$$

Remark 1: An adaptive algorithm based on sliding mode motion is proposed to dynamically adjust the sliding mode coefficient, which not only ensures the existence and stability of the sliding surface, but also makes the system rapidly converge to the sliding mode surface with small overshoot. Moreover, the algorithm is simple and easy to implement.

By subtracting (2) from (6), the error equation of current state is

$$\begin{cases} \frac{d}{dt}\tilde{i}_\alpha = -\frac{R_s}{L_s}\tilde{i}_\alpha - \frac{1}{L_s}\tilde{e}_\alpha - \frac{k_\alpha(t)}{L_s}H(S_\alpha) \\ \frac{d}{dt}\tilde{i}_\beta = -\frac{R_s}{L_s}\tilde{i}_\beta - \frac{1}{L_s}\tilde{e}_\beta - \frac{k_\beta(t)}{L_s}H(S_\beta) \end{cases} \tag{9}$$

where $\tilde{e}_\alpha = \hat{e}_\alpha - e_\alpha, \tilde{e}_\beta = \hat{e}_\beta - e_\beta$ are error signals of the back EMF.

Choosing the following Lyapunov function:

$$V = \frac{1}{2}\mathbf{S_n}^T\mathbf{S_n} + \frac{1}{2\eta}\tilde{\mathbf{k}}_\mathbf{n}^\mathbf{T}(t)\tilde{\mathbf{k}}(t) \tag{10}$$

with$0 < \eta < K_0 L_s$, and differentiating (10) yields

$$\begin{aligned} \dot{V} = S_\alpha \dot{S}_\alpha - \frac{1}{\eta}(K^* - k_\alpha(t))\dot{k}_\alpha(t) \\ + S_\beta \dot{S}_\beta - \frac{1}{\eta}(K^* - k_\beta(t))\dot{k}_\beta(t). \end{aligned} \tag{11}$$

Defining notation

$$\begin{cases} \dot{V}_\alpha = S_\alpha \dot{S}_\alpha - \frac{1}{\eta}(K^* - k_\alpha(t))\dot{k}_\alpha(t) \\ \dot{V}_\beta = S_\beta \dot{S}_\beta - \frac{1}{\eta}(K^* - k_\beta(t))\dot{k}_\beta(t). \end{cases} \tag{12}$$

Then, (11) becomes $\dot{V} = \dot{V}_\alpha + \dot{V}_\beta$. Noting that $\dot{V}_\alpha$ and $\dot{V}_\beta$ are similar and have no coupling relationship, so only $\dot{V}_\alpha$ is analyzed as follows.

From (4), (5), (7), and (9), the equation of $\dot{V}_\alpha$ is derived as

$$\begin{aligned} \dot{V}_\alpha &= S_\alpha \dot{S}_\alpha - \frac{1}{\eta}(K^* - k_\alpha(t))\dot{k}_\alpha(t) \\ &= \left(\chi - \frac{R_s}{L_s}\right)\tilde{i}_\alpha S_\alpha - \frac{S_\alpha}{L_s}(\tilde{e}_\alpha + k_\alpha(t)H(S_\alpha)) \\ &\quad - \frac{K_0\,|S_\alpha|}{\eta}(K^* - k_\beta(t)) \\ &\leq \left(\chi - \frac{R_s}{L_s}\right)\tilde{i}_\alpha S_\alpha + \left(-\frac{S_\alpha \tilde{e}_\alpha}{L_s} - \frac{|S_\alpha|}{L_s}K^*\right) \\ &\quad + |S_\alpha|\,(K^* - k_\beta(t))\left(\frac{1}{L_s} - \frac{K_0}{\eta}\right). \end{aligned} \tag{13}$$

Based on (4), the first term of (13) yields

$$\left(\chi - \frac{L_s}{R_s}\right)\tilde{i}_\alpha S_\alpha = \left(\chi - \frac{L_s}{R_s}\right)\left(\tilde{i}_\alpha \tilde{i}_\alpha + \chi \tilde{i}_\alpha \int_0^t \tilde{i}_\alpha d\tau\right) \leq 0. \tag{14}$$

Moreover, assume$K^* > |\tilde{e}_\alpha|$, the second term of (13) yields

$$-\frac{S_\alpha \tilde{e}_\alpha}{L_s} - \frac{|S_\alpha|}{L_s}K^* < 0. \tag{15}$$

From (8) and$\eta < K_0 L_s$, the last term of (13) yields

$$|S_\alpha|\,(K^* - k_\beta(t))\left(\frac{1}{L_s} - \frac{K_0}{\eta}\right) \leq 0. \tag{16}$$

So, (13) yields

$$\begin{aligned} \dot{V}_\alpha \leq \left(\chi - \frac{R_s}{L_s}\right)\tilde{i}_\alpha S_\alpha - \left(\frac{S_\alpha \tilde{e}_\alpha}{L_s} + \frac{|S_\alpha|}{L_s}K^*\right) \\ + |S_\alpha|\,(K^* - k_\beta(t))\left(\frac{1}{L_s} - \frac{K_0}{\eta}\right) \leq 0. \end{aligned} \tag{17}$$

Similarly, assume$K^* > |\tilde{e}_\beta|$, we can obtain

$$\dot{V}_\beta < 0. \tag{18}$$

Therefore, when

$$K^* > \max\{|\tilde{e}_\alpha|, |\tilde{e}_\beta|\} \tag{19}$$

from (17) and (18), we can get

$$\dot{V} = \dot{V}_\alpha + \dot{V}_\beta < 0 \tag{20}$$

which guarantees the reaching condition of the sliding mode.

Remark 2: Generally, in order to ensure the stability of SMO, the gain of sliding mode is set relatively large, for example, $k > \max\{|e_\alpha|, |e_\beta|\}$ in [28], which leads to large chattering. In this research, only $K^* > \max\{|\tilde{e}_\alpha|, |\tilde{e}_\beta|\}$ is needed, and the value of sliding mode coefficients can adapt to the variations of the sliding mode surface, which guarantees the stability of sliding mode as well as reduces chattering.

Once the system reaches the sliding mode surface, i.e.,

$$\mathbf{S_n} = \begin{bmatrix} S_\alpha \\ S_\beta \end{bmatrix} = \tilde{\mathbf{i}}_\mathbf{s} + \chi \int_0^t \tilde{\mathbf{i}}_\mathbf{s} d\tau = 0$$

by the equivalent principle of sliding mode control, (9) can be simplified as

$$\begin{cases} \tilde{e}_\alpha = (\chi L_s - R_s)\tilde{i}_\alpha \\ \tilde{e}_\beta = (\chi L_s - R_s)\tilde{i}_\beta. \end{cases} \tag{21}$$

Remark 3: Based on a new sliding mode current observer, the proposed IASMO method is used to obtain the error of back EMF instead of the estimated back EMF, which means that the sliding mode gain coefficient is smaller and the chattering will be further reduced.

B. Design of Back EMF Observer

Let $\xi \triangleq \chi L_s - R_s$, so (21) can be rewritten as

$$\begin{cases} \tilde{e}_\alpha = \xi \tilde{i}_\alpha \\ \tilde{e}_\beta = \xi \tilde{i}_\beta. \end{cases} \tag{22}$$

It can be seen from (22) that the error of back EMF in stationary reference frame can be obtained by observing the error of the currents.

Recalling (3), the derivative of back EMF is expressed as

$$\begin{aligned} \frac{d}{dt}e_\alpha &= \frac{d}{dt}(-\omega_e \psi_f \sin\theta_e) \\ &= -\psi_f \sin\theta_e \frac{d}{dt}\omega_e - (\omega_e \psi_f \cos\theta_e)\omega_e. \end{aligned} \tag{23}$$

Usually the sampling frequency of current is very high and the change rate of speed is far less than that of current in the process of rotor operation, so it can be considered that $\frac{d}{dt}\omega_e = 0$ in a sampling period. Then, (23) can be further expressed as

$$\begin{cases} \frac{d}{dt}e_\alpha \approx -\omega_e e_\beta \\ \frac{d}{dt}e_\beta \approx \omega_e e_\alpha. \end{cases} \tag{24}$$

According to (22) and (24), the observed equation of back EMF can be reconstructed as

$$\begin{cases} \frac{d}{dt}\hat{e}_\alpha = -\hat{\omega}_e\hat{e}_\beta - l\xi\tilde{i}_\alpha \\ \frac{d}{dt}\hat{e}_\beta = \hat{\omega}_e\hat{e}_\alpha - l\xi\tilde{i}_\beta \\ \frac{d}{dt}\hat{\omega}_e = \tilde{e}_\alpha\hat{e}_\beta - \tilde{e}_\beta\hat{e}_\alpha \end{cases} \tag{25}$$

where parameter l is a positive constant, which determines the convergence rate of the observer. By combining (22) and (25), we obtain

$$\begin{cases} \frac{d}{dt}\hat{e}_\alpha = -\hat{\omega}_e\hat{e}_\beta - l\tilde{e}_\alpha \\ \frac{d}{dt}\hat{e}_\beta = \hat{\omega}_e\hat{e}_\alpha - l\tilde{e}_\beta \\ \frac{d}{dt}\hat{\omega}_e = \tilde{e}_\alpha\hat{e}_\beta - \tilde{e}_\beta\hat{e}_\alpha. \end{cases} \tag{26}$$

Constructing a positive definite Lyapunov function as

$$V = \frac{1}{2}(\tilde{e}_\alpha^2 + \tilde{e}_\beta^2 + \tilde{\omega}_e^2) \tag{27}$$

and differentiating (27) yields

$$\begin{aligned} \dot{V} &= \tilde{e}_\alpha\frac{d}{dt}\tilde{e}_\alpha + \tilde{e}_\beta\frac{d}{dt}\tilde{e}_\beta + \tilde{\omega}_e\frac{d}{dt}\tilde{\omega}_e \\ &= -l\left(\tilde{e}_\alpha^2 + \tilde{e}_\beta^2\right) + \hat{\omega}_e\left(-\tilde{e}_\alpha\hat{e}_\beta + \tilde{e}_\beta\hat{e}_\alpha + \frac{d}{dt}\tilde{\omega}_e\right) \\ &\quad + \omega_e\left(\tilde{e}_\alpha e_\beta - \tilde{e}_\beta e_\alpha - \frac{d}{dt}\tilde{\omega}_e\right). \end{aligned} \tag{28}$$

From (28), we obtain

$$\dot{V} = -l(\tilde{e}_\alpha^2 + \tilde{e}_\beta^2) \le 0. \tag{29}$$

Based on the above proof, the back EMF observer (25) is stable, and the stability of the observer is only related to the motor parameters and has nothing to do with the external disturbances. The estimated rotor speed can track the change of back EMF signal when the system converges and maintains in a boundary layer.

The IASMO will force $\hat{e}_\alpha, \hat{e}_\beta$ to converge toe_α, e_β, respectively, and then quickly make $\hat{\omega}_e$ converge to ω_e until error is zero. Therefore, the IASMO can reduce the error caused by chattering, and improve the accuracy of the rotor position.

According to (26), the estimated value of$\hat{e}_\alpha$,$\hat{e}_\beta$, and $\hat{\omega}_e$ can be obtained, so the rotor angle can be obtained directly by integrating the angular velocity

$$\hat{\theta}_e = \int \hat{\omega}_e dt. \tag{30}$$

Remark 4: When the traditional arctangent function method is used to estimate the rotor position, the high-frequency noise of the system will be directly introduced into the division operation of arctangent function, resulting in further enlargement of the deviation. Also, the proposed method is different from the phase-locked loop technique extracting rotor position by back EMF signal, which may lead to complex calculation and low accuracy. This method not only has advantages of simple design and less computation, but also overcomes the disadvantage of arctangent function which is more sensitive to high-frequency noise.

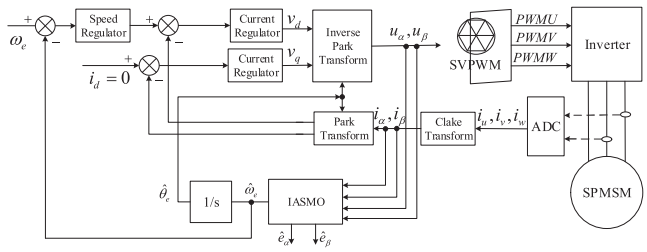

Fig. 2. Block diagram of sensorless vector control system under the IASMO for SPMSM.

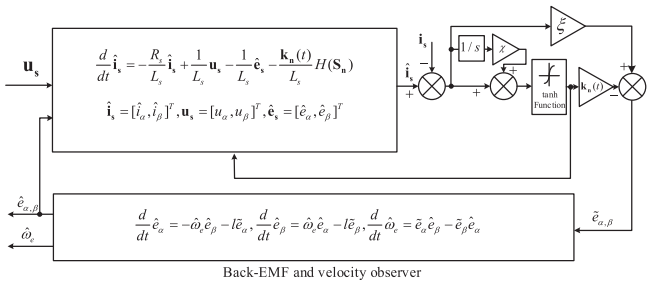

Fig. 3. Structural diagram of the IASMO.

TABLE I
MAIN PARAMETERS AND VALUES OF THE SPMSM

Items	Values	Parameters	Values
Stator resistance R_S	0.2Ω	K(0)	60
Stator inductance L_S	95μH	K_0	150
Flux linkage Ψ_f	0.25 Wb	η	0.005
Rate Voltage U_N	30 V	τ	0.0001
Rotational inertia J	0.00094kg·m^2	χ	15
Switching frequency f	10000 Hz	a	8
Pole pairs P_n	8	l	200

IV. SIMULATION AND EXPERIMENTAL ANALYSIS

A. Simulation Analysis

According to the analysis of the IASMO in the preceding sections, a simulation model of the sensorless control system under the IASMO method for SPMSM is established as Fig. 2. Based on the platform of MATLAB/Simulink, structural diagram of the proposed IASMO with back EMF and velocity observer is constructed as Fig. 3. The parameters of SPMSM in simulation and experiment are shown in Table I as follows.

For comparision, the parameters of the current loop and the speed loop under the IASMO and ASMO methods are the same, and the simulation time is also consistent. For PI parameters of the current regulator, the proportional gain K_p is 0.76 and integral gain K_i is 1600. In traditional ASMO, the value of

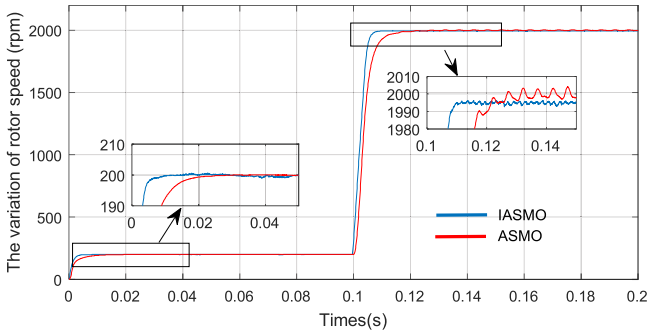

Fig. 4. Variation of rotor speed of system under the IASMO and ASMO when the rotor is stepping up from 0 to 200 to 2000 r/min, respectively.

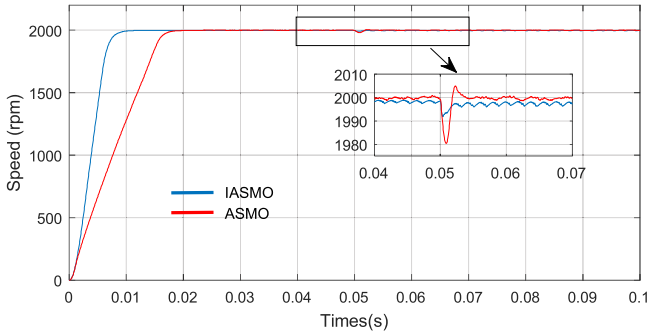

Fig. 5. Speed response of system under the IASMO and ASMO when the disturbance is added suddenly, respectively.

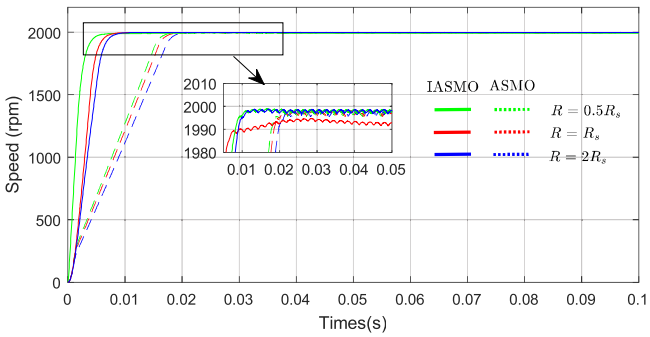

Fig. 6. Speed response of system with the change of stator resistance under the IASMO and ASMO, respectively.

sliding mode gain K is 240. IASMO and ASMO control methods based on $i_d = 0$ vector control strategy are implemented to SPMSM systems under different situations shown as Figs. 4–7, respectively.

Fig. 4 shows the variation of rotor speed of system under the IASMO and ASMO when the rotor speed steps up from 0 to 200 to 2000 r/min, respectively. It shows that the convergence time under the ASMO is relatively short. And when the rotor speed rises from 0 r/min to the given speed, the speed rotor of the system under the IASMO converges rapidly without overshoot. On the other hand, when the rotor speed reaches steady state, the speed error of system under IASMO is about 0.12%, but the speed error of the system under IASMO is about 0.25 %. In addition, when the rotor encounters sudden change of velocity,

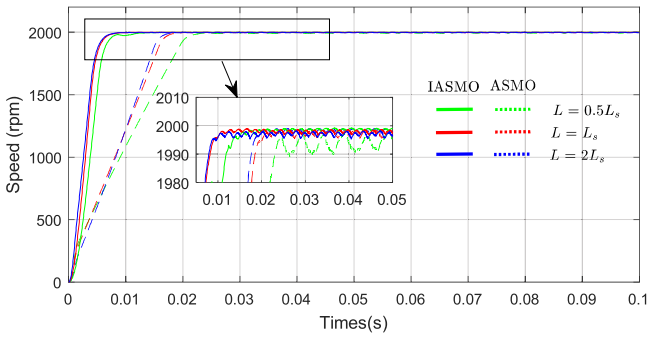

Fig. 7. Speed response of system with the change of winding inductance under the IASMO and ASMO, respectively.

the adaptive sliding mode gain can dynamically adapt to the variations of the rotor speed.

Accroding to the analysis of sliding mode control theory, the capability of the antidisturbance of the system mainly depends on the sliding mode gain. In other words, when the system encounters disturbance, it can recover to the steady state quickly by adaptively increasing the gain of sliding mode control. Fig. 5 shows the speed response of the system under the IASMO and ASMO at 2000 r/min when the disturbance $T_L = 0.5\,\mathrm{N{\cdot}m}$ is added suddenly at 0.05 s, respectively. It can be seen that the recovery time is 2 and 4.5 ms by using the IASMO and ASMO, respectively.

Although the SPMSM system based on ASMO has a certain adaptive ability, the tracking performance of the rotors will be correspondingly poor when the stator resistances and winding inductances of the motor changes. In order to demonstrate the adaptive ability of the IASMO under different applications, such as the sudden the change of the stator inductances and winding resistances, some simulations are carried out in Figs. 6 and 7.

Figs. 6 and 7 indicate the contrastive results under the IASMO and ASMO when internal parameters of the SPMSM change, respectively. It can be seen that the speed response of system under the IASMO are almost independent of the internal parameters of the motor, and the convergence speed is faster, which verified the good adaptability and effectiveness of the proposed control strategy. From Figs. 6 and 7, it is seen that the convergence time decreases with increase of L_s when R_s is unchanged within a certain range; conversely, the convergence time increases with increase of R_s when L_s is unchanged.

By comparing the simulation results of the two methods, it can be seen that sensorless control system under the IASMO not only has the advantage over the traditional ASMO in tracking characteristics, but also has good adaptability to multikinds of loads and the rapid response to the rotor speed. Moreover, owing to the adaptive performance of the sliding mode gain, the chattering of the sliding mode control system under the IASMO is smaller than that of the ASMO method.

B. Experimental Analysis

To further testify the performance of the IASMO, the experimental platform of the sensorless vector control system is constructed as shown in Fig. 8 and the performance of the

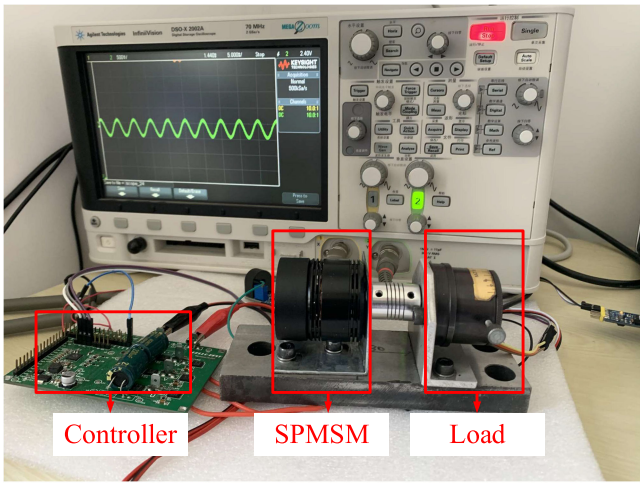

Fig. 8. Experimental platform of the sensorless vector control system.

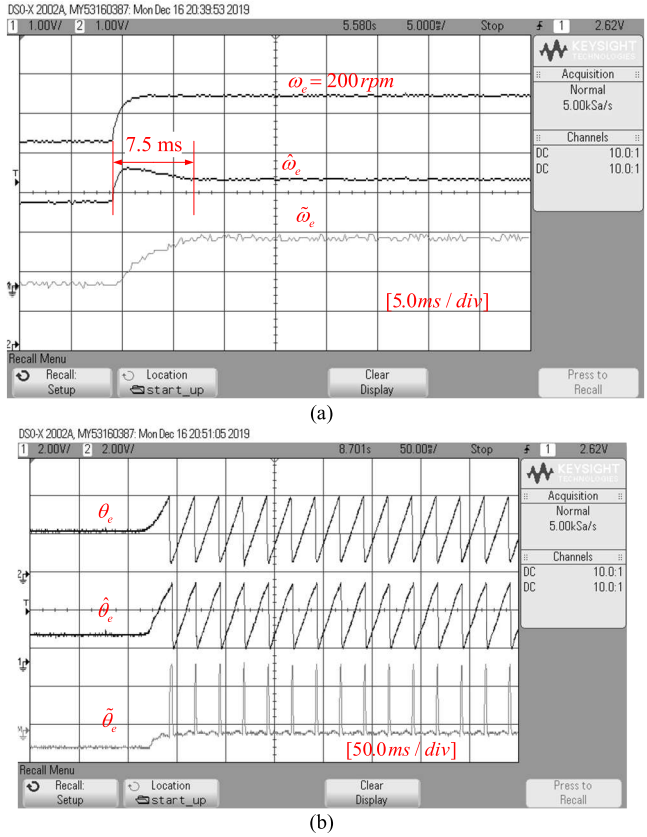

Fig. 9. Start-up process of system under the traditional ASMO. (a) Rotor speed. (b) Rotor position.

proposed algorithm is analyzed. And in this study, the sensorless vector control strategy is implemented by using PAC5223 microprocessor which integrates a 32-b microcontroller unit (MCU) of ARM Cortex-M0 with 50 MHz clock frequency. Moreover, the MCU possesses abundant peripheral resources, such as multiplex pulsewidth modulation (PWM) driver with dead zone, high-speed analog-to-digital converter (ADC). The SPMSM is driven by a conventional voltage-source inverter and an integrated power module by means of space vector PWM technique. Two-phase currents of stator windings (i_a, i_b) are measured from the resistors and then sent to the MCU via two ADCs. In addition, the direct current bus voltage in the inverter is measured and sent to the ADC, which is essential to further optimize the performance of the control system.

1) Start-Up Experiment: Fig. 9 represents the start-up process of system under the traditional ASMO when the rotor rises from static state to the given speed. The given speed of the motor rotor is set to 200 r/min without load, and the value of sliding mode gain K is 240. Fig. 9(a) represents the speed change when the rotor speed steps from 0 to 200 r/min. And the top, middle, and bottom waveform signals show the actual, estimation, and error of the rotor speed, respectively. It takes 7.5 ms from 0 to 200 r/min and the steady-state speed error is 1.4 r/min. The three oscillograms in Fig. 9(b) represent the actual value θ_e, estimated value $\hat{\theta}_e$, and error of rotor position $\tilde{\theta}_e$, respectively. It can be seen that the rotor position of system under ASMO has certain phase deviation.

Fig. 10 shows the same start-up experiment of system under the IASMO as Fig. 9. Fig. 10(a) shows the start-up process of system under the IASMO method when the rotor speed is from 0 to 200 r/min. Fig. 10(b) shows the change of the rotor position when the rotor speed increases from 0 to 200 r/min. Compared with the experimental results from Fig. 9, when the rotor rises from 0 to 200 r/min, the start-up time of system under the IASMO is 5.2 ms, but the start-up time of system under the traditional ASMO is 7.5 ms. In addition, the overshoot of the rotor speed of system under the IASMO is less than that of the ASMO method. And the rotor position of the system under the IASMO has almost no phase deviation. The experimental result manifests that the IASMO is superior to the traditional ASMO in starting performance.

2) Accelerated Experiment: In Figs. 11 and 12, some experimental results are given to manifest the acceleration performance of the system under the ASMO and IASMO, respectively. Fig. 11 shows the acceleration process of the system under the traditional ASMO when the rotor speed changes suddenly from 200 to 2000 r/min. From top to bottom, Fig. 11(a) shows the reference electrical angular velocity ω_e, the actual electrical angular velocity $\hat{\omega}_e$, and the error of electrical angular velocity $\tilde{\omega}_e$, respectively. It can be seen that the transition time of rotor speed from 200 to 2000 r/min is about 325 ms, and the speed error is about 8 r/min during this time. In Fig. 11(a) and (b), the change time of the rotor position and back EMF are both about 325 ms when the rotor speed increases from 200 to 2000 r/min. Moreover, the value of the back EMF will increase with the increase of rotor speed.

Fig. 12 indicates the same accelerated experiment under the IASMO as Fig. 11. These three waveforms represent the changes of rotor speed, rotor position, and back EMF, respectively. Compared with the experimental results in Fig. 11(a), Fig. 12(a) shows that it only takes 200 ms for the rotor speed change from 200 to 2000 r/min. Similarly, the change time of rotor position is also 200 ms when the rotor speed changes from

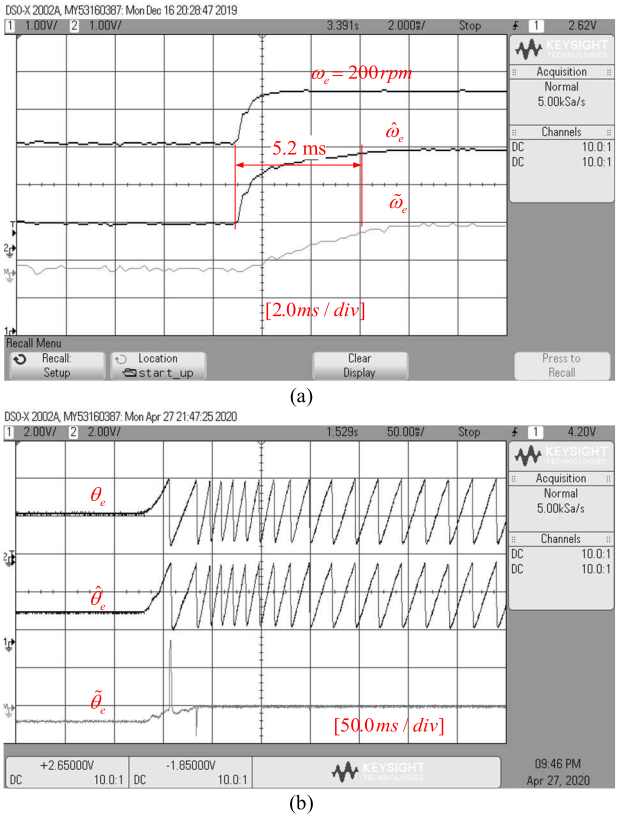

Fig. 10. Start-up process of system under IASMO. (a) Rotor speed. (b) Rotor position.

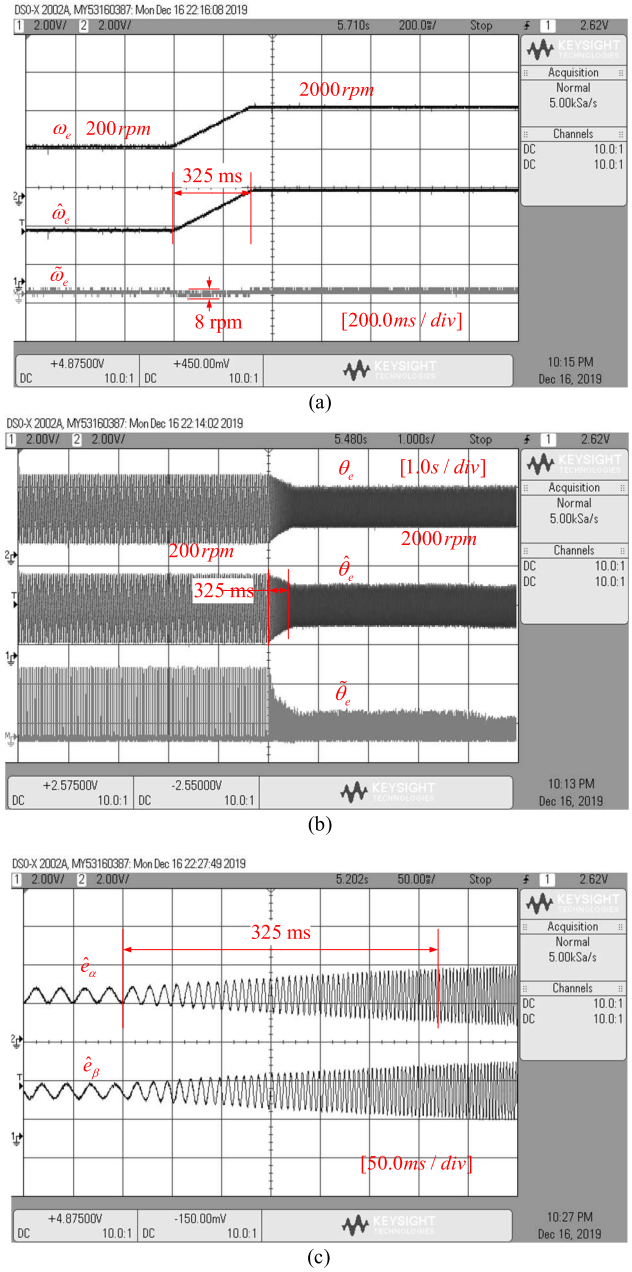

Fig. 11. Acceleration process of system under the conventional ASMO when the rotor is stepping up from 200 to 2000 r/min. (a) Rotor speed. (b) Rotor position. (c) Estimated back EMF of $\alpha - \beta$ axis.

200 to 2000 r/min. Obviously, the response speed of the system under IASMO is increased by 38.5% comparing with ASMO method. Furthermore, the response time of the back EMF under the IASMO is about 225 ms instead of 325 ms under the traditional ASMO. These comparative experiments further show that system under the IASMO method has faster acceleration performance than that of traditional ASMO.

3) Steady-State Experiment: Fig. 13 shows the steady-state experiment waveforms under the traditional ASMO when the motor rotor runs stably at 200 and 2000 r/min, respectively. Fig. 13(a) and (b) shows the speed and position waveforms when the rotor runs at middle speed of 200 r/min, respectively. And Fig. 13(c) and (d) shows the speed and position waveforms when the rotor runs at a high speed of 2000 r/min, respectively. As shown in Fig. 13(a)–(d), when the rotor speed runs stably at 200 r/min, the speed error is about 2 r/min and the position error is about 4.8°; when the rotor speed runs at 2000 r/min, the speed error is about 7.8 r/min and the position error is about 6.7°.

By comparison, Fig. 14 shows the speed and position waveforms of the system under the IASMO when the rotor runs stably at 200 and 2000 r/min, respectively. From Fig. 14(a) and (b), when the rotor runs stably at 200 r/min, the speed error is about 1.5 r/min and the position error is about 3.2°. From Fig. 14(c) and (d), when the rotor runs at a high speed of 2000 r/min, the rotor speed and position errors are 5.6 r/min and 4.3°, respectively.

From Fig. 13(a) and (b) and Fig. 14(a) and (b), when the rotor runs stably at a middle speed of 200 r/min, the speed fluctuation and system chattering under the IASMO are smaller than that of traditional ASMO. Similarly, from Fig. 13(c) and (d) and Fig. 14(c) and (d), when the rotor runs at a high speed of 2000 r/min, the speed fluctuation and system chattering under the IASMO are also smaller than that of traditional ASMO. Further comparative performance indexes on the two algorithms are shown in Table II.

According to the experimental data in Table II, it can be concluded that the sensorless vector control technology system under the IASMO has better performance than that of traditional ASMO at middle and high speeds, such as chattering suppression, good adaptability, fast convergence speed, and stability.

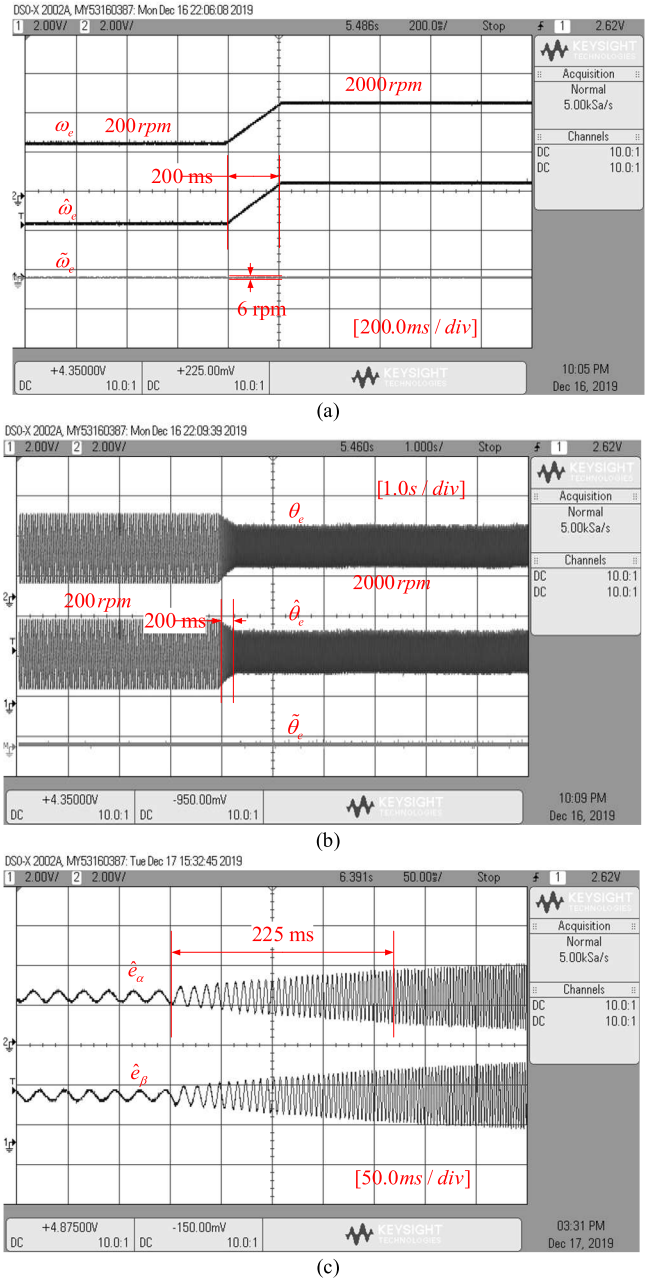

Fig. 12. Acceleration process of system under the IASMO when the rotor is stepping up from 200 to 2000 r/min. (a) Rotor speed. (b) Rotor position. (c) Estimated back EMF of $\alpha - \beta$ axis.

TABLE II
EXPERIMENT COMPARISON PERFORMANCES OF IASMO AND ASMO

Rotor speed	Items	ASMO	IASMO
200 rpm	Convergence time	7.5 ms	5.2 ms
	speed steady-state error	2.4 rpm	1.5 rpm
	Overshoot	5 rpm	0.2 rpm
	Angle error	4.8°	3.2°
2000 rpm	Convergence time	325 ms	200 ms
	speed steady-state error	7.8 rpm	5.6 rpm
	Overshoot	1 rpm	0.6 rpm
	Angle error	6.7°	4.3°

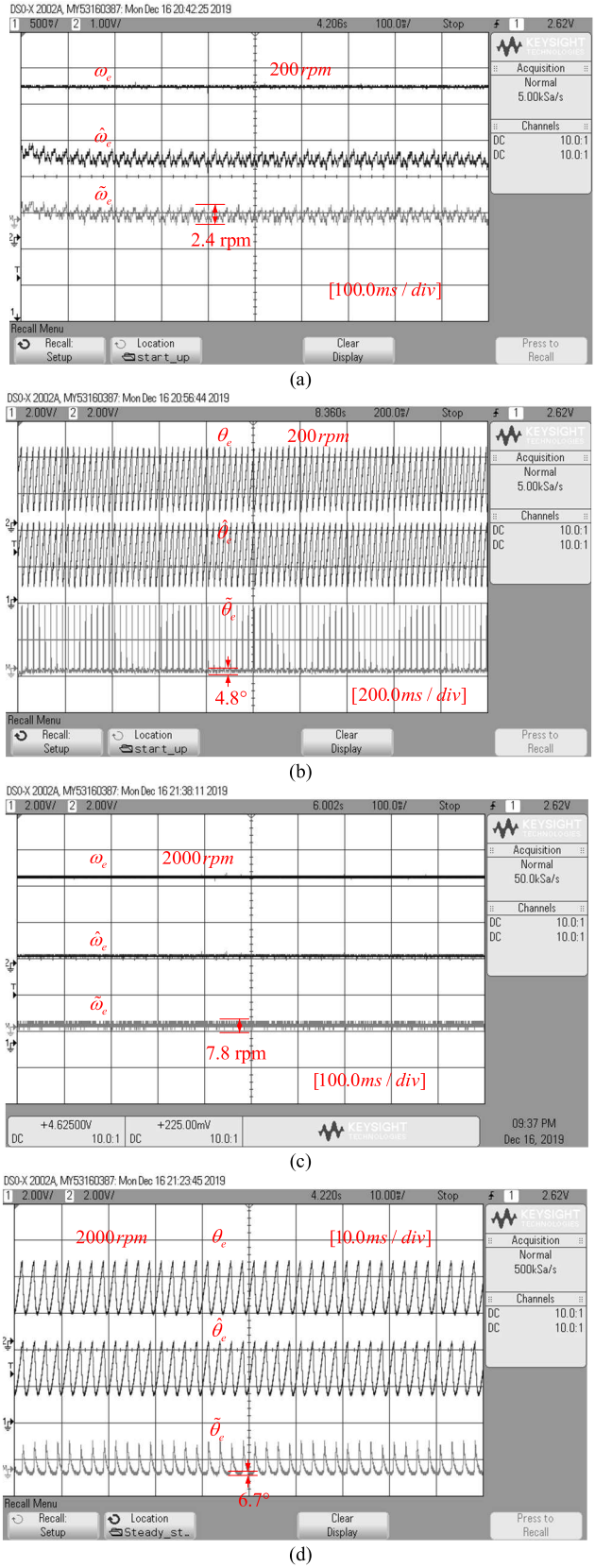

Fig. 13. Steady-state waveforms of the system under the ASMO at 200 and 2000 r/min, respectively. (a) Rotor speed at 200 r/min. (b) Rotor position at 200 r/min. (c) Rotor speed at 2000 r/min. (d) Rotor position at 2000 r/min.

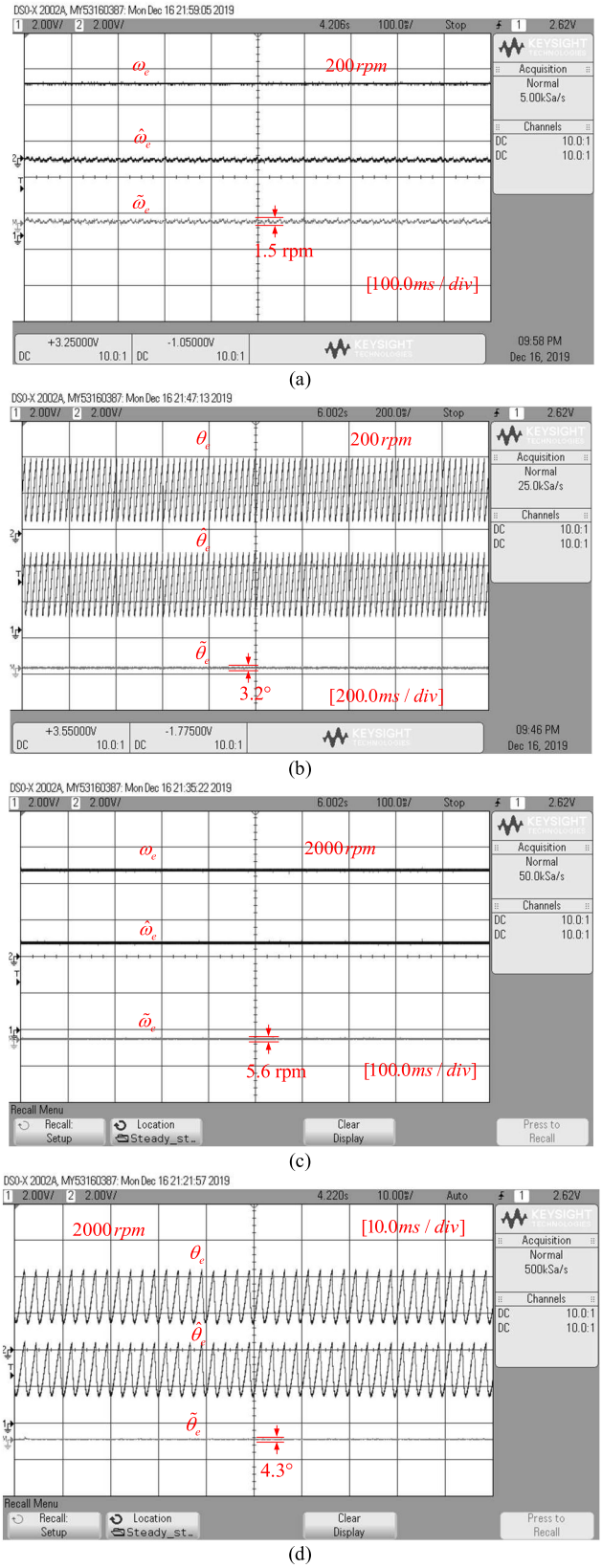

Fig. 14. Steady-state waveforms of the system under IASMO at 200 and 2000 r/min, respectively. (a) Rotor speed at 200 r/min. (b) Rotor position at 200 r/min. (c) Rotor speed at 2000 r/min. (d) Rotor position at 2000 r/min.

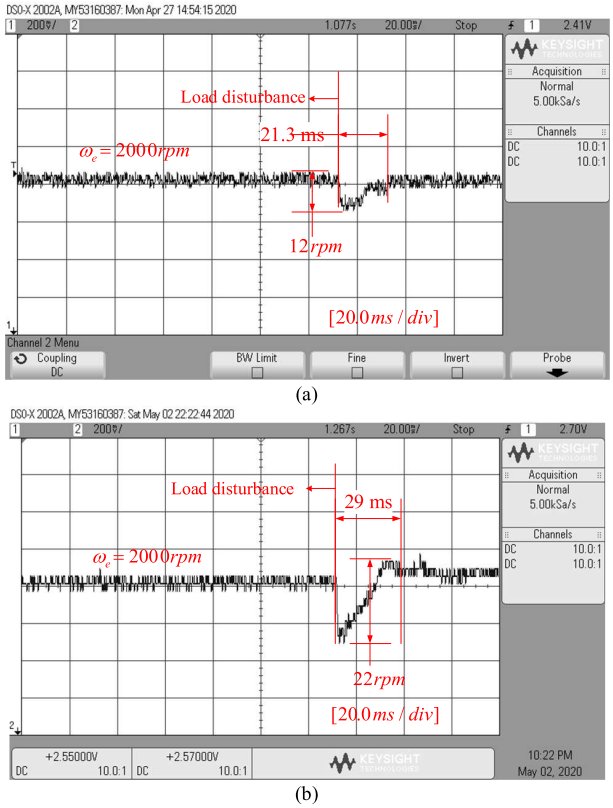

Fig. 15. Rotor speed response at 2000 r/min in the case of sudden disturbance load. (a) Rotor speed response of the system under IASMO. (b) Rotor speed response of the system under ASMO.

4) Antidisturbance Experiment: In order to testify the antidisturbance performance of system under the IASMO method at high speed 2000 r/min, comparative experiments with two cases (case 1: Sudden disturbance load; case 2: Change of three-phase stator winding resistance) are implemented, and shown in Figs. 15 and 16, respectively.

Fig. 15 shows the rotor speed response of the system under the IASMO and ASMO method at high speed 2000 r/min when the disturbance load $T_L = 0.5\,\mathrm{N}\cdot\mathrm{m}$ is suddenly added, respectively. It can be seen from Fig. 15(a) that the recovery time of the speed under the IASMO is 21.3 ms and the speed drop is 12 r/min. However, Fig. 15(b) shows that the recovery time under the ASMO method is 29 ms and the speed drop is 22 r/min.

Fig. 16 shows the rotor speed response and phase current of the system under the IASMO and ASMO methods when the motor winding is connected in series with a resistance of 0.2 Ω, respectively. As shown in Fig. 16(a), the response time of the system under the IASMO is 235 ms when the speed steps from 0 to 2000 r/min, but the response time in Fig. 16(b) is 400 ms. Furthermore, Fig. 16(c) and (d) shows that the A-phase current waveforms of the system under the IASMO are more stable than that of the ASMO. From Figs. 15 and 16, it can be concluded that the proposed IASMO method has better antidisturbance performance than the ASMO method.

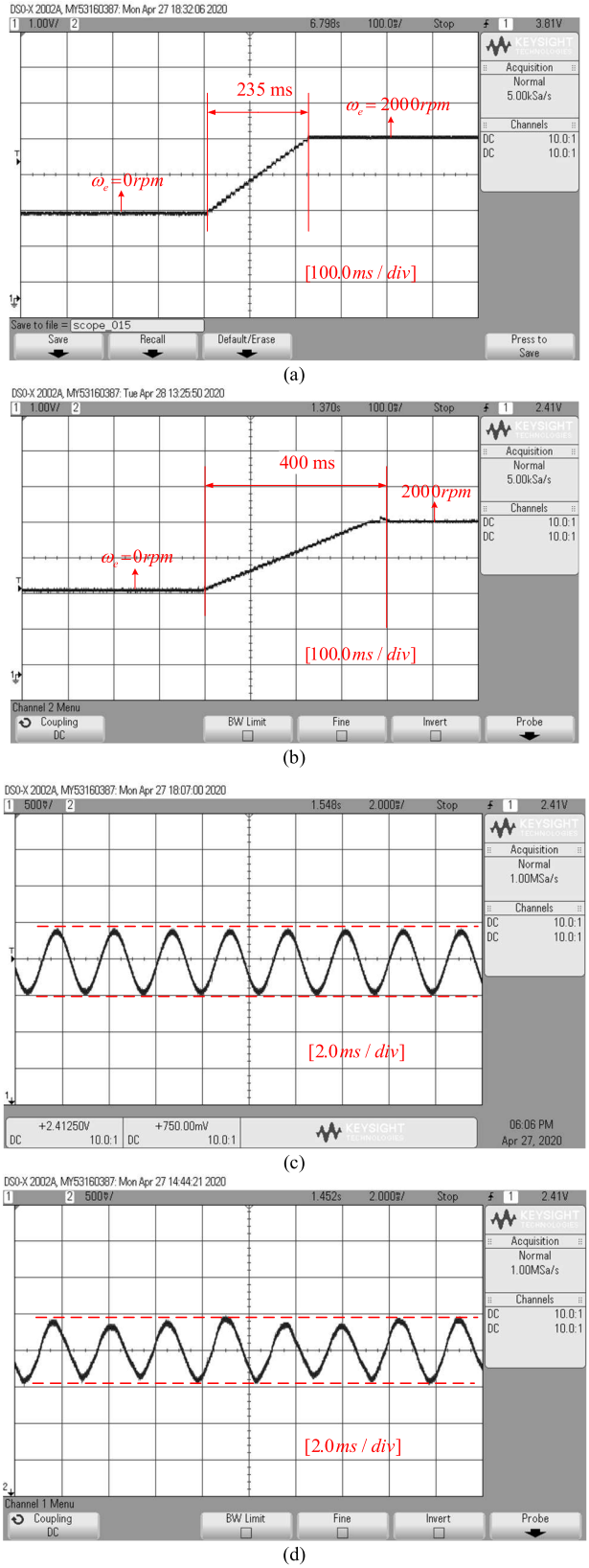

(a) (b) (c) (d)

Fig. 16. Rotor speed response and phase current in case of the change of three-phase stator winding resistance. (a) Rotor speed of the system under IASMO. (b) Rotor speed of the system under ASMO. (c) A-phase current (1 A/div) of the system under IASMO. (d) A-phase current (1 A/div) of the system under ASMO.

V. Conclusion

This article proposes a sensorless FOC strategy based on an IASMO algorithm for the SPMSM rotor. First, this article proposes an IASMO based on a new sliding mode current observer, which estimates the error of back EMF instead of the value of the back EMF used by state-of-the-art ones, and it is different from the traditional sliding mode current observer. Second, an adaptive gain algorithm is proposed to dynamically adjust the sliding mode coefficient, which can make the system rapidly converge to the sliding mode surface with small overshoot phenomenon. Meanwhile, the algorithm is simple and feasible. Third, the back EMF observer can obtain the speed of the rotor directly by the error of the back EMF, and then get the position of the rotor by integral operation. Moreover, the stability of the IASMO and back EMF observer is proved by the Lyapunov method. Finally, start-up experiment, accelerated experiment, steady-state experiment, and antidisturbance experiment are implemented to show the effectiveness of the proposed strategy.

References

[1] I. I. Abdalla, T. Ibrahim, and N. B. M. Nor, "Development and optimization of a moving-magnet tubular linear permanent magnet motor for use in a reciprocating compressor of household refrigerators," *Int. J. Elect. Power Energy Syst.*, vol. 77, pp. 263–270, May 2016.

[2] T. C. Lin and Z. Q. Zhu, "Sensorless operation capability of surface-mounted permanent-magnet machine based on high-frequency signal injection methods," *IEEE Trans. Ind. Appl.*, vol. 51, no. 3, pp. 2161–2171, May/Jun. 2015.

[3] J. Hu, J. Zou, F. Xu, Y. Li, and Y. Fu, "An improved PMSM rotor position sensor based on linear hall sensors," *IEEE Trans. Magn.*, vol. 48, no. 11, pp. 3591–3594, Nov. 2012.

[4] S. Kim, C. Choi, K. Lee, and W. Lee, "An improved rotor position estimation with vector-tracking observer in PMSM drives with low-resolution hall-effect sensors," *IEEE Trans. Ind. Electron.*, vol. 58, no. 9, pp. 4078–4086, Sep. 2011.

[5] H. H. Chou, Y. S. Kung, N. V. Quynh, and S. Cheng, "Optimized FPGA design, verification and implementation of a neuro-fuzzy controller for PMSM drives," *Math. Comput. Simul.*, vol. 90, no. 2, pp. 28–44, Apr. 2013.

[6] B. Alecsa, M. N. Cirstea, and A. Onea, "Simulink modeling and design of an efficient hardware-constrained FPGA-based PMSM speed controller," *IEEE Trans. Ind. Inform.*, vol. 8, no. 3, pp. 554–562, Aug. 2012.

[7] W. C. Chi and M. Y. Cheng, "Implementation of a sliding-mode-based position sensorless drive for high-speed micro permanent-magnet synchronous motors," *Int. Soc. Autom. Trans.*, vol. 53, no. 2, pp. 444–453, 2014.

[8] X. Song, B. Han, S. Zheng, and S. Chen, "A novel sensorless rotor position detection method for high-speed surface PM motors in a wide speed range," *IEEE Trans. Power Electron.*, vol. 33, no. 8, pp. 7083–7093, Aug. 2018.

[9] G. Xie, K. Lu, S. K. Dwivedi, J. R. Rosholm, and F. Blaabjerg, "Minimum-voltage vector injection method for sensorless control of PMSM for low-speed operations," *IEEE Trans. Power Electron.*, vol. 31, no. 2, pp. 1785–1794, Feb. 2016.

[10] M. Seilmeier and B. Piepenbreier, "Sensorless control of PMSM for the whole speed range using two-degree-of-freedom current control and HF test current injection for low-speed range," *IEEE Trans. Power Electron.*, vol. 30, no. 8, pp. 4394–4403, Aug. 2015.

[11] O. C. Kivanc and S. B. Ozturk, "Sensorless PMSM drive based on stator feedforward voltage estimation improved with MRAS multiparameter estimation," *IEEE/ASME Trans. Mechatronics*, vol. 23, no. 3, pp. 1326–1337, Jun. 2018.

[12] N. K. Quang, N. T. Hieu, and Q. P. Ha, "FPGA-based sensorless PMSM speed control using reduced-order extended Kalman filters," *IEEE Trans. Ind. Electron.*, vol. 61, no. 12, pp. 6574–6582, Dec. 2014.

[13] Z. Wang, Y. Zheng, Z. Zou, and M. Cheng, "Position sensorless control of interleaved CSI Fed PMSM drive with extended Kalman filter," *IEEE Trans. Magn.*, vol. 48, no. 11, pp. 3688–3691, Nov. 2012.

[14] G. H. B. Foo, X. Zhang, and D. M. Vilathgamuwa, "A sensor fault detection and isolation method in interior permanent-magnet synchronous motor drives based on an extended Kalman filter," *IEEE Trans. Ind. Electron.*, vol. 60, no. 8, pp. 3485–3495, Aug. 2013.

[15] D. D. Reigosa, D. Fernandez, Z. Zhu, and F. Briz, "PMSM magnetization state estimation based on stator-reflected PM resistance using high-frequency signal injection," *IEEE Trans. Ind. Appl.*, vol. 51, no. 5, pp. 3800–3810, Sep./Oct. 2015.

[16] M. Seilmeier, S. Ebersberger and B. Piepenbreier, "HF test current injection-based self-sensing control of PMSM for low- and zero-speed range using two-degree-of-freedom current control," *IEEE Trans. Ind. Appl.*, vol. 51, no. 3, pp. 2268–2278, May/Jun. 2015.

[17] J. R. Domínguez, A. Navarrete, M. A. Meza, A. G. Loukianov, and J. Cañedo, "Digital sliding-mode sensorless control for surface-mounted PMSM," *IEEE Trans. Ind. Inform.*, vol. 10, no. 1, pp. 137–151, Feb. 2014.

[18] D. Liang, J. Li, and R. Qu, "Sensorless control of permanent magnet synchronous machine based on second-order sliding-mode observer with online resistance estimation," *IEEE Trans. Ind. Appl.*, vol. 53, no. 4, pp. 3672–3682, Jul./Aug. 2017.

[19] H. Liu and S. Li, "Speed control for PMSM servo system using predictive functional control and extended state observer," *IEEE Trans. Ind. Electron.*, vol. 59, no. 2, pp. 1171–1183, Feb. 2012.

[20] S. Qu, X. Xia, and J. Zhang, "Dynamics of discrete-time sliding-mode-control uncertain systems with a disturbance compensator," *IEEE Trans. Ind. Electron.*, vol. 61, no. 7, pp. 3502–3510, Jul. 2014.

[21] S. Qu, X. Xia, and J. Zhang, "Dynamical behaviors of an Euler discretized sliding mode control systems," *IEEE Trans. Autom. Control*, vol. 59, no. 9, pp. 2525–2529, Sep. 2014.

[22] S. Lin and W. Zhang, "An adaptive sliding-mode observer with a tangent function-based PLL structure for position sensorless PMSM drives," *Int. J. Elect. Power Energy Syst.*, vol. 88, pp. 63–74, 2017.

[23] H. Lee and J. Lee, "Design of iterative sliding mode observer for sensorless PMSM control," *IEEE Trans. Control Syst. Technol.*, vol. 21, no. 4, pp. 1394–1399, Jul. 2012.

[24] H. Kim, J. Son, and J. Lee, "A high-speed sliding-mode observer for the sensorless speed control of a PMSM," *IEEE Trans. Ind. Electron.*, vol. 58, no. 9, pp. 4069–4077, Sep. 2011.

[25] S. A. Davari, D. A. Khaburi, F. Wang, and R. M. Kennel, "Using full order and reduced order observers for robust sensorless predictive torque control of induction motors," *IEEE Trans. Power Electron.*, vol. 27, no. 7, pp. 3424–3433, Jul. 2012.

[26] O. Wallmark and L. Harnefors, "Sensorless control of salient PMSM drives in the transition region," *IEEE Trans. Ind. Electron.*, vol. 53, no. 4, pp. 1179–1187, Jun. 2006.

[27] M. Preindl and E. Schaltz, "Sensorless model predictive direct current control using novel second-order PLL observer for PMSM drive systems," *IEEE Trans. Ind. Electron.*, vol. 58, no. 9, pp. 4087–4095, Sep. 2011.

[28] Z. Qiao, T. Shi, Y. Wang, Y. Yan, C. Xia, and X. He, "New sliding-mode observer for position sensorless control of permanent-magnet synchronous motor," *IEEE Trans. Ind. Electron.*, vol. 60, no. 2, pp. 710–719, Feb. 2013.

[29] H. Lee and V. I. Utkin, "Chattering suppression methods in sliding mode control systems," *Annu. Rev. Control*, vol. 31, no. 2, pp. 179–188, 2007.

[30] D. Liang, J. Li, R. Qu, and W. Kong, "Adaptive second-order sliding-mode observer for PMSM sensorless control considering VSI nonlinearity," *IEEE Trans. Power Electron.*, vol. 33, no. 10, pp. 8994–9004, Oct. 2018.